The reemergence of the winter sea surface temperature tripole in the North Atlantic from ocean reanalysis data

Pavel A. Sukhonos[1, *] (0000-0002-1427-4286), Michael A. Alexander[2, **] (0000-0001-9646-6427)

[1]Institute of Natural and Technical Systems, Sevastopol, Russia

[2]NOAA Physical Sciences Laboratory, Boulder, CO, USA

*e-mail: pasukhonis@mail.ru

**e-mail: michael.alexander@noaa.gov

Abstract

Multiple ocean reanalyses and objective analyses are used to study the reemergence of the large–scale pattern of winter sea surface temperature anomalies (SSTAs) in the North Atlantic (15°N–70°N 80°W–8°W). The dominant SSTAs pattern in winter forms under the North Atlantic Oscillation forcing and have a tripole structure with anomalies of one sign in the subtropics and the opposite sign in the tropics and high latitudes. Empirical orthogonal function (EOF) analysis indicates that the dominant mode of interannual variability in the summer seasonal thermocline (~65–90 m in August–September) has also a tripole structure. The reemergence mechanism is evaluated by correlating the time series of the leading pattern of ocean temperature anomalies in the summer seasonal thermocline with SSTA over the course of the year. It is shown that the tripole in the summer seasonal thermocline is most strongly related to SSTAs in the previous March–April (explains ~15% of the variance), when the upper mixed layer (UML) of the North Atlantic is deepest. During summer, the SSTA variance explained by this EOF decreases, reaching a minimum of 5–6% in August–September. With the UML deepening in the subsequent autumn–winter, this value increases, reaching two–thirds of the initial signal.

Key words: Sea Surface Temperature; Reemergence; Tripole; North Atlantic

Introduction

Winter sea surface temperature anomalies (SSTAs) at mid-latitudes have a tendency to repeat from one winter to the next, while SSTAs during the intervening summer fades within two to three months. This behavior of SSTAs is closely related to the seasonal evolution of the depth of the upper mixed layer (UML) of the ocean (Namias and Born 1970). The process where SSTAs formed in the deep UML in one winter are maintained below the shallow UML in summer and return to the surface when the mixed layer deepens in the following fall and winter has been called the «reemergence mechanism» (Alexander and Deser 1995). This hypothesis was confirmed by observational data, reanalyses and studies using models (e.g., Alexander and Deser 1995; Deser et al. 2003; Frankignoul et al. 2021; Sukhonos and Diansky 2021). The reemergence mechanism appears to occur over a substantial portion of the world's oceans (Byju et al. 2018). The exception is the central and eastern parts of the tropical latitudes of the Pacific Ocean, where El Niño–Southern Oscillation variability predominates.

In the North Atlantic, there are two regions with a pronounced manifestation of the SSTA reemergence (Hanawa and Sugimoto 2004). These are the Sargasso Sea and the northeast North Atlantic regions. The exact boundaries of these regions may vary due to different criteria and methods for distinguishing the SSTA reemergence. These regions are confined to subtropical and subpolar cells with opposite signs on the tripole structure of the leading empirical orthogonal function (EOF) of SSTA in the North Atlantic (Watanabe and Kimoto 2000; Timlin et al. 2002; Sukhonos and Diansky 2021). These authors found evidence of the SSTA reemergence in these regions and showed that it can make a significant contribution to the SSTA formation in the North Atlantic on an interannual to decadal scale. An analysis of the SSTA autocorrelation coefficients in the World Ocean, obtained from satellite data for the period 1981–2018, showed that the winter SSTA reemergence is most pronounced in the region of the subpolar gyre south of Greenland (Bulgin et al. 2020). Frankignoul et al. (2021) examined the SSTA reemergence in the North Atlantic (20°–50° N 70°–20° W) based on

correlation analysis with and without considering geostrophic advection. They found that the SSTA reemergence occurs in 31 of the 57 five–degree squares and possibly in 11 more squares. It should be noted that the secondary peak in the SSTA autocorrelation function may not be associated with the SSTA reemergence mechanism. This peak can be caused by other physical processes, for example, atmospheric forcing or non–local processes in the upper layer of the ocean. Deviations of the SSTA autocorrelation functions from that of a red–noise process might also be a result of residuals in de–seasonalizing the data (Geiss et al. 2020). Note that in the North Atlantic, small regions were also identified in which there is no SSTA reemergence. These are the central part of the North Atlantic, where intense subduction is observed (de Coëtlogon and Frankignoul 2003), and the North Atlantic Madeira Mode Water formation area (30°–38° N 15°–25° W), due to vigorous salt–finger type convection (Sugimoto and Hanawa 2005a). The above studies have shown that in some regions of the North Atlantic, including those associated with individual cells of the tripole structure, the timing and structure of the reemerging signal may vary and the SSTA reemergence may not occur.

The data on winter SSTA in the North Atlantic show that on interannual time scales, a tripole structure prevails with anomalies of the same sign in the tropics and high latitudes and of the opposite sign in the subtropics. This tripole pattern repeats from one winter to the next and is greatly diminished at the ocean surface during the summer. The SSTA tripole reemergence has been studied in a number of studies. For example, for this purpose Watanabe and Kimoto (2000), Zhao et al. (2005) and Cassou et al. (2007) used simple ocean models; the de Coëtlogon and Frankignoul (2003) results are based only on SST and Taws et al. (2011) analyzed just one year. Preservation of the SSTA tripole structure from winter-to-winter is associated with the seasonal cycle of UML depth and is due to the process of reemergence of anomalies. The North Atlantic Oscillation (NAO) during the winter season creates a tripole structure of the SSTA within the deep winter UML. These anomalies persist beneath the UML during the spring–summer period within a stably stratified seasonal thermocline. The summer seasonal

thermocline is isolated from the atmosphere by the formation of a new shallow UML, which is formed due to an increase in the influx of solar radiation and a seasonal weakening of the surface winds. Thermal stratification prevents mixing, and the UML depth is small in summer. In the subsequent autumn–winter period, the slow UML deepening begins again. This is due to the difference in the stratification of the upper ocean layer during these periods: from almost neutral stratification during the period of maximum cooling of the UML to strong stratification during the period of maximum heating of the UML. The temperature anomalies formed last winter and located in the summer thermocline are entrained into the UML, affecting the SST (Hurrell and Deser 2010). Thus, the large-scale tripole structure of winter SSTA in the North Atlantic persists from winter-to-winter due to the reemergence mechanism. The reemerging SSTAs may affect the winter atmospheric circulation over the North Atlantic and NAO variability (Czaja and Frankignoul 2002; Cassou et al. 2007; Taws et al. 2011; Buchan et al. 2014; Grist et al. 2019).

The goal of this paper is to examine the reemergence of the large-scale SSTA tripole in the North Atlantic using long-term data from several reanalyses and objective analyses. Using a wide array of independent datasets, enables us to examine the robustness of the reemergence of a basin–wide pattern and the extent to which reanalyses are able to represent it.

Data and processing method

The data used in the paper are monthly mean values of upper ocean temperature from objective analysis datasets of EN.4.2.2 for the period 1945–2020 (Good et al. 2013) with a set of corrections by Gouretski and Reseghetti (2010) and ISHII for the period 1945–2012 (Ishii et al. 2003) and from ocean reanalysis datasets, including the: Simple Ocean Data Assimilation (SODA) version 2.1.6 for the period 1958–2008 (Carton and Giese 2008), Ocean Reanalysis System 4 (ORA-S4) for the period 1958–2014 (Balmaseda et al. 2013), Ocean Reanalysis System 3 (ORA-S3) for the period 1959–2011 (Balmaseda et al. 2008), German contribution of the Estimating the Circulation and Climate of the Ocean project

version 3S6m (GECCO3) for the period 1948–2018 (Köhl 2020), Geophysical Fluid Dynamics Laboratory (GFDL) reanalysis for the period 1961–2015 (Chang et al. 2013), Global Ocean Data Assimilation System (GODAS) for the period 1980–2021 (Behringer and Xue 2004), Global Ocean Eddy-Permitting Physical Reanalysis version 4 (GLORYS2V4) for the period 1993–2015 (Garric et al. 2017), Ocean Reanalysis System 5 (ORA-S5) for the period 1979–2018 (Zuo et al. 2019), Simple Ocean Data Assimilation (SODA) version 3.12.2 for the period 1980–2017 (Carton et al. 2018). Monthly averages of the NAO index for the period 1950–2021 taken from the website of the National Center for Climate Prediction, USA (https://www.cpc.ncep.noaa.gov/products/precip/CWlink/pna/nao.shtml).

The datasets have different horizontal and vertical resolutions. All calculations are performed at the initial spatial resolution of the data. To remove low–frequency variability, third–order polynomials were first subtracted from the time series of the data at each grid point and the NAO index. Such a filtering procedure makes it possible to exclude the influence of the long–term global increase in ocean temperature and the Atlantic Multidecadal Oscillation. For example, periodicities of ~40 years or more are removed for datasets with ~70 year duration. From the GODAS, GLORYS2V4, ORA-S5 and SODA3.12.2 time series, only first–order polynomials (linear trends) were subtracted because of their short duration. The polynomial coefficients were calculated by the least–squares method.

We analyze the reemergence of the dominant pattern of temperature anomalies in the North Atlantic, using EOF and correlation analysis. The leading EOF is computed using the covariance matrix in which the variance at each grid point in a month has been normalized by the average standard deviation of temperature at all grid points in the domain during that month. The statistical significance of the correlation coefficients is assessed using a one–tailed Student's *t*–test based on the effective sample size as described in (Bretherton et al. 1999).

The percentage of variance of temperature anomalies, explained by the time coefficient of the leading EOF (principal component), is estimated by the formula:

$$\sum_{i=1}^{N} r_i^2 \sigma_i^2 \,/\, \sum_{i=1}^{N} \sigma_i^2 \,, \qquad (1)$$

where r is the correlation coefficient between the time series of temperature anomalies and the time coefficient of the EOF, σ is the standard deviation of the temperature anomalies, i indicates an individual grid point, and N is the total number of grid points.

Results and their analysis

As a first step, we examine the reemergence process in the Sargasso Sea (25°–35° N 65°–45° W) and the northeast Atlantic (35°–60° N 45°–8° W). These regions correspond to the subtropical and subpolar cells with opposite signs in the tripole pattern of the leading EOF. Temperature anomalies were averaged over these regions and EOFs computed in the time–depth plane following Timlin et al. (2002). The EOF for the Sargasso Sea region was calculated as follows. The temperature values on a spatial grid from specified levels in the 0–300 m layer and 15 months (January to the next March) is the observational vector for each year (corresponding to a spatial map in traditional EOF analyses) of the available period. The EOF calculation for the northeast Atlantic region was carried out similarly, except using a 0–550 m layer.

Correlations between temperature anomalies within a 15–month interval (January–March of the next year) for both the Sargasso Sea and northeast Atlantic, identified using EOF analysis from GECCO3 data for the period 1948–2017, are shown in Fig. 1. In these regions the leading EOF describes 54% and 71% of the variability in the time–depth plane, respectively. In the Sargasso Sea region the correlation coefficients at the surface (0–30 m) decrease from May to November, while the correlation coefficients at depths (70–150 m) almost never decrease from March to January of the following year. In the northeast Atlantic region the UML temperature anomalies formed during the period of its greatest winter deepening in February–March persist at depths of 100–250 m. The EOF patterns for these regions, in all of the datasets, are shown in the supplemental material (Figs. S1 and S2). Averaging all datasets, the leading EOF in the Sargasso Sea and in the northeast Atlantic explain 48% and 65% of the variance, respectively. Note that when calculating according to the EN4 data for the period 1980–2020, the leading

EOF pattern in the time–depth plane changes little, but the percentage of the explained variance increases by almost a quarter compared to the calculation for the period 1945–2020.

Thus, in both regions, the leading EOFs demonstrate the formation of temperature anomalies within the UML during the period of its greatest winter deepening in March and their persistence at depths of 50–200 m throughout the year with their gradual deepening by the end of the 15–month period. This is fully consistent with the concept of the local SSTA reemergence. Note that the process under consideration explains half of the temperature variance in the 0–300 m layer in the Sargasso Sea region and two thirds of the temperature variance in the 0–550 m layer in the northeast Atlantic region.

In winter, at high latitudes, due to convective mixing, the seasonal thermocline is practically absent and is observed only at latitudes less than 30° N. The origin of the seasonal thermocline in most of the World Ocean begins with the warming of the upper layer, and it reaches its maximum development at high latitudes (50°–70° N) in August. During the summer warming of the upper ocean layer, the temperature gradient between the UML and the underlying water increases. In August–September, a temperature jump layer – the summer seasonal thermocline, forms under the shallow UML. This layer is characterized by an increased temperature gradient. The vertical temperature gradient for the specified months at depth z was calculated by the central difference method – the ratio of the temperature difference between the underlying and overlying layers ($t_{z+1} - t_{z-1}$) to twice the layer thickness ($2 \bullet \Delta z$). Then, the depth of the maximum gradient was determined from the profiles of the vertical temperature gradient at each grid point. This value, computed from the data used, is given in Table 1. The layer of the summer seasonal thermocline is important for the analysis of the SSTA tripole reemergence. This is the depth for which the largest explained variance in SSTA is recorded in the previous February–March–April, when the UML in most of the North Atlantic has a maximum depth. For such a large area (15°–70° N), the UML and depth of the maximum vertical temperature gradient can vary. It depends not

only on the geographical features of the region, but also on the vertical resolution of a specific dataset. The generalized analysis for all datasets used showed that for the most of the North Atlantic, the summer seasonal thermocline is located in the 65–90 m layer. In order to analyze how sensitive the SSTA reemergence to depth selection, we estimated the percent variance of the SSTA in the North Atlantic explained by the leading EOF in the layers above and below depth of the maximum temperature gradient. These depths are also shown in Table 1.

Under SSTA we define temperature anomalies at the top level of each dataset (0 m – for ISHII, GLORYS2V4 and ORA-S5, 6 m – for GECCO3 and 5 m – for other data sets). Let us further consider the relationship between temperature anomalies on the ocean surface and in the summer seasonal thermocline in the North Atlantic (15°–70° N, 80°–8° W). Setting the southern and northern boundaries of the region to 20° N and 65° N gave similar results (not shown). The EOF calculation is based on temperature anomalies in the summer seasonal thermocline averaged over August and September, as the results using August and September separately are similar (not shown).

The leading EOF of temperature anomalies in August–September averaged in the layer of the summer seasonal thermocline, which depth is given in Table 1, is used to determine the dominant mode of variability in the summer seasonal thermocline. The spatial structure of this EOF, as illustrated by the GECCO3 ocean reanalysis in the 68–82 m layer, is shown in Fig. 2 as a correlation between the time coefficient and temperature anomalies over the available period at individual grid points. The spatial structure of the leading EOF of temperature anomalies in the summer seasonal thermocline in the North Atlantic according to almost all datasets used is the tripole pattern (Fig. S3). In subtropical and subpolar latitudes, temperature changes are of the same sign, and in midlatitudes – the opposite. The magnitude of the correlation coefficients in absolute value exceeds 0.4 in subtropical latitudes east of 60° W, in the vicinity of the Gulf Stream and in the subpolar gyre with maxima greater than 0.6 in the subtropical and subpolar poles of the tripole. Note that the blue area in the Gulf Stream extension region is the

most pronounced according to the GECCO3 and GODAS data, although this area is less pronounced in other data sets. Slight differences in the Gulf Stream extension region may be due to the ability of the analysis/reanalysis to accurately depict the western boundary current.

The variance of temperature anomalies in the summer seasonal thermocline in the North Atlantic, explained by the leading EOF, is given in Table 1. This EOF describes about 14% of the variance of temperature anomalies in August–September in the 65–90 m layer. The variance explained ranges from 7.4% for the SODA2.1.6 reanalysis to 18.9% for the GODAS reanalysis.

The time coefficient of the leading EOF of temperature anomalies in August–September in the summer seasonal thermocline (hereinafter referred to as PC1) shows pronounced interannual and long-term variability. The correlations of PC1 between the different data sets, over the period in which they overlap, are shown in Table 2. High and significant correlation coefficients between them are noted for almost all data sets. This allows us to isolate the tripole pattern in the summer seasonal thermocline in the North Atlantic from several long-term data sets and identify its relationship with the SSTA tripole pattern. Periodicities of the interannual scale coincide with typical NAO variability (Gámiz-Fortis et al. 2002; Hurrell and Deser 2010).

The correlation coefficients between PC1 and the winter NAO index are shown in Table 3. With seasonal averaging of the NAO index, the correlations become higher for almost all datasets, reaching values that are significant at the 95% confidence level. Correlations with the NAO index for the ORA-S4 data also increase, but are still not significant. The exceptions are the SODA2.1.6 and GODAS data. For these datasets, this tendency is reversed. Significant and positive coefficients from most data sets confirm the conclusions about the connection between the leading temperature pattern in the summer seasonal thermocline and the state of the leading mode of atmospheric variability in the previous winter in the North Atlantic.

The spatial distributions of the correlation coefficients between PC1 and SSTA at individual grid points in the North Atlantic during the previous March and subsequent September and November are shown in Fig. 3, as illustrated by the GECCO3 reanalysis. Areas of relatively high correlation coefficients (exceeding 0.4 in absolute value) are used to assess the strength of the relationship between the large-scale structure of temperature anomalies in the summer seasonal thermocline and SSTA in spring and autumn. The correlations between PC1 and SSTA in March have a tripole structure with values exceeding 0.4 in tropical latitudes east of 60°W, in the vicinity of the Gulf Stream and in the subpolar gyre (Fig. 3a). The values of the correlation coefficients exceed 0.6 in the central part of the subtropical Atlantic, the Gulf Stream region and the eastern part of the subpolar gyre, which indicates a strong relationship between SSTA in spring and temperature anomalies in the summer seasonal thermocline. On the whole, this spatial distribution of correlation coefficients agrees very well with the spatial structure of the leading EOF of temperature anomalies in the summer seasonal thermocline (Fig. 2). The value of correlations between PC1 and SSTA in September is small over most of the North Atlantic (Fig. 3b), but increases by November (Fig. 3c), exceeding 0.4 in the vicinity of the Gulf Stream and in the subpolar gyre.

Thus, the SSTA tripole structure in the North Atlantic in March and November is closely related to the tripole structure of temperature anomalies in the summer seasonal thermocline. A similar result was obtained for the dominant mode of SSTA variability in the north Pacific Ocean (Alexander et al. 1999).

The percent variance of the SSTA explained by PC1 in the North Atlantic as a function of calendar month from previous January to the following April was calculated using Eq. 1 and shown in Fig. 4. The percent of the SSTA variance, explained by PC1, increases from about 10% in January to 15% in March–April, and then decreases in each of the following months, reaching a minimum of 5–6% in August–September. By November, it recovers to 8–10%, and then gradually decreases until April of the following year. With the exception of SODA2.1.6

300 reanalysis, all of the data sets show a peak in the previous winter, a late summer
301 minimum, and a secondary peak in the following fall or winter. The amplitude and
302 month of the increase in variance varies between data sets. The SODA2.1.6 data
303 exhibits low explained variance (~3%) that is invariant with the seasons. The
304 increase in variance explained in the following cold season is very strong (nearly
305 15%) in the GODAS reanalysis, but it occurs later in the winter than most other
306 data sets. The reemerging signal in GODAS during autumn is almost the same as
307 in the previous spring (92–94% of the amplitude of the reemerging signal in
308 March). Most datasets show the returning branch of the reemergence process is
309 weaker than its formation due to ocean processes such as subduction and mixing
310 with deeper waters in summer/fall, plus uncorrelated atmospheric forcing in the
311 following fall/winter. The reemerging signal, as suggested by the increase in
312 variance explained in the following fall, is fairly strong in the GECCO3 and
313 GLORYS2V4 reanalyses and ISHII analysis but weaker in the EN.4.2.2 analysis.
314 The EN.4.2.2 objective analysis data in the North Atlantic are very noisy.
315 All calculations for this dataset were repeated for the entire available period
316 (1945–2020) and for the period 1980–2020. When calculating for the period 1980–
317 2020, the percent variance of the SSTA increase in all months and become
318 commensurate with the other datasets (excluding the 35–45 m layer). In the winter
319 months, the percent variance of the SSTA is 18%, and in the summer and autumn–
320 winter months, the percent variance of the SSTA is 9%. This suggests that the
321 reemergence mechanism accounts for half the variance associated with the leading
322 EOF in the following winter. The maximum of the SSTA reemergence signal
323 occurs in December. When calculating for the layer above the summer seasonal
324 thermocline (35–45 m), the SSTA reemergence signal is not expressed. When
325 calculated for the period 1945–2020 (as shown in Fig. 4, red line), the percent
326 variance of the SSTA is almost two times smaller than when computed for the
327 period 1980–2020. The intensity of the SSTA reemergence signal increases in the
328 period when the data is less noisy. At the same time, the form of time dependence
329 on the calendar months is preserved for these two periods.

Analysis of the sensitivity of the SSTA tripole reemergence to the depth selection showed that most datasets represent this process above and below the summer seasonal thermocline layer. However, there are exceptions. The SSTA tripole pattern reemergence signal is not expressed in the layer above the thermocline (~30–47 m) in the ISHII objective analysis, SODA2.1.6 and GODAS reanalyses. In this layer the reemergence signal in GODAS in the following March is 115% of the peak value in the previous March. In the layer below the thermocline (~120–135 m) the reemergence signal does not appear in the SODA2.1.6, ORA-S3 and GODAS reanalyses. For the first two datasets, the reemerging signal in this layer explains little variance (3%) irrespective of season. For the GODAS reanalysis, returning signal from this layer in the following March is 94% of the peak value in the previous March, which is much larger than what is expected from reemergence alone.

The average percent variance of the SSTA in the North Atlantic explained by PC1 in the layer above, in and under the summer seasonal thermocline are shown in Fig. 5. The average includes all data sets except those described above. The highest percent variance of the SSTA (~16%) explained by PC1 was obtained for winter SSTA values (February–March–April). For the layer above the thermocline, the winter values of the percent variance of the SSTA are significantly lower, and the summer values are significantly higher. The percent SSTA variance explained by this layer in summer (August–September) is higher because it interacts more with the thin UML. For the layer under the thermocline, the values of the percent variance of the SSTA are generally lower in all months. Thus, the North Atlantic SSTA tripole pattern, formed in winter, is sequestered in the seasonal thermocline in summer with little persistence at the surface in the summer.

We now examine the evolution of North Atlantic temperature anomalies as a function of time and depth by calculating the percent of variance of temperature anomalies in the upper ocean explained by the time coefficient of the leading EOF. Figure 6 shows the percent variance of temperature anomalies explained by PC1

using the GECCO3 reanalysis data. Values are shown from previous January to the following April for the period 1948–2017 at 16 levels in the upper 400 m. The leading EOF describes 13.2% of the total variance in the 0–400 m layer and more than 11% of the variance of temperature anomalies in the 0–250 m layer in the first winter, below 35 m in summer and at the ocean surface in the following December. The leading EOF of temperature anomalies in the summer seasonal thermocline explains less than 8% of the variance of SSTA in July–September compared to more than 17% at depths of 50 to 100 m during the same months. The recurring temperature anomalies are weaker partially because the subsurface temperature anomalies over the 16 month period, from January to April of the following year, diffuse or are subducted into the deeper layers of the ocean (up to 300 m).

We now consider an additional correlation analysis. The SSTA values at each grid point in a month were first normalized by the basin-wide standard deviation for that month and then the EOF of SSTAs was calculated separately for each month of the year. Basin-wide standard deviation in a month is the average standard deviation of SSTA at all points in the domain during that month. The spatial structure of the leading EOF of SSTA in winter months has a pronounced tripole pattern. The correlation coefficients between the time coefficient of the leading EOF of the SSTA, computed separately for each month of the year, and PC1 were calculated and shown in Fig. 7. For datasets with duration of about 70 years, a correlation coefficient of 0.4 or more can be considered significant at the 99% confidence level. Most of the data sets show a high correlation between PC1 with the time coefficient of the leading EOF for winter SSTA. The correlation coefficient is above 0.6. This relationship weakens in summer (correlation coefficient 0.3–0.4) and recovers again by December (correlation coefficient 0.5 ± 0.1). This is consistent with the concept of the reemergence of the SSTA tripole pattern and with the analysis presented in Fig. 4. The correlation coefficients according to GODAS and SODA2.1.6 data are not high. Analysis of Figs. 4 and 7 and Tables 2 and 3 shows that the SODA2.1.6 (underestimated) and GODAS

(overestimated) reanalyses does not seem to have a reemergence mechanism of the large–scale SSTA tripole pattern in the North Atlantic.

As indicated by the percent variance explained (Fig. 4), the reemerging signal peaks in November for GECCO3 and SODA3.12.2, in December for all other datasets and in January for ORA-S3 and ORA-S5. SODA2.1.6 and GODAS were deemed to not have a reliable reemerging signal. The maximum correlation in the following autumn–winter according to Fig. 7 for 9 datasets is observed in November for GECCO3, December for all other datasets and January for ORA-S3. Most of the datasets show that the maximum signal of the reemergence of the SSTA tripole in the North Atlantic occurs in December, as confirmed by averaging over all datasets except SODA2.1.6 and GODAS (Fig. 5).

Conclusions

The reemergence of the large-scale pattern of winter SSTA in the North Atlantic (15°N–70°N 80°W–8°W) is analyzed using multiple ocean reanalyses and objective analyses of various durations. The main method is decomposition into EOFs and correlation analysis. The following can be distinguished as the main results.

The large-scale SSTA tripole structure, formed in the previous winter period due to NAO forcing, extends through the deep winter UML. It is greatly diminished at the ocean surface in late summer–early autumn, but reoccurs at the ocean surface in following late autumn–early winter with the subsequent deepening of the UML (Fig. 8). In summer this SSTA tripole pattern is sequestered in the seasonal thermocline (~ 65–90 m in August–September). The recurring temperature anomalies are weaker, since the subsurface temperature anomalies for 16 months (January–April next year) also diffuse or propagate into the deeper layers of the ocean (up to 300 m). In addition, atmospheric anomalies in the second winter are likely to be different from those in the previous winter and thus, would act to obscure the reemerging anomalies. The UML depth small seasonality and some processes in the upper layer of the ocean, such as advection and subduction, could also diminish the reemergence mechanism (Watanabe and Kimoto 2000;

Timlin et al. 2002; de Coëtlogon and Frankignoul 2003; Frankignoul et al. 2021). Removing long–term trends is important for analyzing year–to–year variability. This procedure may also remove some part of reemergence, which could contribute to lower frequency variability (Newman et al. 2016). The focus here is on local reemergence, which means that temperature anomalies are generated and reemerge at the same location, as opposed to remote reemergence, where the areas of formation and occurrence of SSTA can be separated in space due to movement of waters in the upper layer of the ocean (de Coëtlogon and Frankignoul 2003; Sugimoto and Hanawa 2005b). The remote reemergence might be underestimated by the EOF approach and requires additional study.

The dominant mode of temperature variability in the summer seasonal thermocline is a tripole structure. Part of the variance of temperature anomalies in August–September, explained by the leading EOF after removing lower frequency variability using a 3rd degree polynomial, varies from 11 to 18% in the different data sets. A significant and positive correlation for different datasets was found between the time coefficients of this EOF and the NAO index in previous winter. Indicating that large–scale atmospheric forcing in the previous winter plays an important role in driving the temperature variability in the summer seasonal thermocline in the North Atlantic.

The time coefficient of the leading EOF of temperature anomalies in the summer seasonal thermocline describes the largest part of the SSTA variance in March–April (about 15%), when the North Atlantic UML is deepest. In the summer months, the part of the SSTA variance decreases, reaching a minimum in August–September (5–6%). In the subsequent autumn–winter period, with the UML deepening, this value increases, reaching two-thirds of the initial value. Watanabe and Kimoto (2000) showed that the magnitude of the observed summer temperature anomalies under the lower boundary of the North Atlantic UML is approximately one third of the magnitude of the previous winter SSTA. The former and latter temperature anomalies are the same sign, consistent with our results.

448 However, the present analysis shows that the reemerging signal is approximately
449 twice as strong (~2/3 to 1/3) than in their study.
450 The correlation between the time coefficient of the EOF of temperature
451 anomalies in the summer seasonal thermocline in August–September and the time
452 coefficient of the leading EOF of SSTA calculated separately for each month of the
453 year is strong during the winter months (correlation coefficient above 0.6). This
454 relationship weakens in summer (correlation coefficient 0.3–0.4) and recovers
455 again by December (correlation coefficient 0.5 ± 0.1). The temperature anomalies
456 in the summer seasonal thermocline that partake in the reemergence mechanism
457 are more strongly associated with SSTA in the previous spring than with SSTA in
458 the following winter.
459 The timing of the reemerging signal varies for different regions of the North
460 Atlantic (Hanawa and Sugimoto 2004; Zhao and Li 2010; Frankignoul et al. 2021).
461 The EOF approach detects coherent patterns by incorporating information in the
462 original anomaly field from all grid points of the study area. Most of the datasets
463 that correctly depict the structure of the SSTA tripole reemergence show the return
464 to the surface reaches a maximum in December.
465 Many factors may contribute to the differences in how reemergence is
466 represented in the different reanalyses. These include the observations that are
467 assimilated, the assimilation system, the atmospheric boundary conditions and the
468 ocean model, including its resolution and parameterizations. The UML depth, a
469 critical variable in the reemergence process, is not assimilated directly but is a
470 diagnostic that depends on the assimilated temperature and salinity profiles and the
471 mixing scheme within the ocean models. Thus, it is not possible to isolate why the
472 reanalyses differ from each other. We note that the GODAS and SODA2.1.6, the
473 oldest data sets used here, were developed more than 15 years ago and thus use
474 older models and assimilation systems. In addition, SODA2.1.6 poorly reproduces
475 the tripole pattern of temperature anomalies in the summer seasonal thermocline
476 (Fig. S3) and has the lowest percent variance explained by the leading EOF (Table
477 1). At the same time, the new SODA3.12.2, unlike its predecessor, does have a

reemergence signal and it is consistent with most of the other reanalyses. The GODAS is based on a quasi–global ocean model (the model domain extends from 75°S to 65°N) and assimilates synthetic salinity profiles (Behringer and Xue 2004). These factors may contribute to inferior representation of the reemergence mechanism.

By using multiple data sets, including several high resolution recently developed reanalyses, we were able to confirm the reemergence of the SSTA tripole. It also provides a test of different ocean analyses and how they represent a process that occurs in much of the North Atlantic. Such an approach could be used for a comprehensive study of other aspects of ocean variability as well and provide information that developers can use to improve future versions of ocean reanalyses.

Acknowledgements: The authors thank the anonymous reviewers for the constructive and insightful comments, which have helped us to improve our manuscript. The authors would like to thank C.-W. Hsu for helpful comments.

Funding: The work of P.S. was supported by Russian Science Foundation (project No. 19–17–00110).

Author contribution: P.S. conceived the study, performed the analysis and wrote the first draft of the manuscript. All authors contributed to the design of the study, interpretation and presentation of results, and writing and revision of the manuscript.

Conflicts of interest: The authors declare no conflict of interest

Data availability: All data used in this study are available from publicly accessible data archives

References

1. Alexander MA, Deser C (1995) A mechanism for the recurrence of wintertime midlatitude SST anomalies. J Phys Oceanogr 25(1):122–137. https://doi.org/10.1175/1520-0485(1995)025<0122:AMFTRO>2.0.CO;2

2. Alexander MA, Deser C, Timlin MS (1999) The reemergence of SST anomalies in the North Pacific Ocean. J Clim 12(8):2419–2433. https://doi.org/10.1175/1520-0442(1999)012<2419:TROSAI>2.0.CO;2

3. Balmaseda MA, Mogensen K, Weaver AT (2013) Evaluation of the ECMWF ocean reanalysis system ORAS4. Q J R Meteorol Soc 139(674):1132–1161. https://doi.org/10.1002/qj.2063

4. Balmaseda MA, Vidard A, Anderson DLT (2008) The ECMWF Ocean Analysis System: ORA-S3. Mon Weather Rev 136(8):3018–3034. https://doi.org/10.1175/ 2008MWR2433.1

5. Behringer DW, Xue Y (2004) Evaluation of the global ocean data assimilation system at NCEP: The Pacific Ocean. Proc. Eighth Symp. on Integrated Observing and Assimilation Systems for Atmosphere, Ocean, and Land Surface. Seattle, WA, Amer. Meteor. Soc. [Available online at http://ams.confex.com/ams/pdfpapers/70720.pdf.]

6. Bretherton CS, Widmann M, Dymnikov VP, Wallace JM, Bladé I (1999) The effective number of spatial degrees of freedom of a time-varying field. J Clim 12(7):1990–2009. https://doi.org/10.1175/1520-0442(1999)012<1990:TENOSD>2.0.CO;2

7. Buchan J, Hirschi JJ, Blaker AT, Sinha B (2014) North Atlantic SST anomalies and the cold North European weather events of winter 2009/10 and December 2010. Mon Weather Rev 142(2):922–932. https://doi.org/10.1175/MWR-D-13-00104.1

8. Bulgin CE, Merchant CJ, Ferreira D (2020) Tendencies, variability and persistence of sea surface temperature anomalies. Scientific reports 10(1):1–13. https://doi.org/10.1038/s41598-020-64785-9

9. Byju P, Dommenget D, Alexander MA (2018) Widespread reemergence of sea surface temperature anomalies in the global oceans, including tropical regions forced by reemerging winds. Geophys Res Lett 45(15):7683–7691. https://doi.org/10.1029/2018GL079137

10. Carton JA, Chepurin GA, Chen L (2018) SODA3: A new ocean climate reanalysis. J Clim 31(17):6967–6983. https://doi.org/10.1175/JCLI-D-18-0149.1

11. Carton JA, Giese BS (2008) A reanalysis of ocean climate using Simple Ocean Data Assimilation (SODA). Mon Weather Rev 136(8):2999–3017. https://doi.org/10.1175/2007MWR1978.1

12. Cassou C, Deser C, Alexander MA (2007) Investigating the impact of reemerging sea surface temperature anomalies on the winter atmospheric circulation over the North Atlantic. J Clim 20(14):3510–3526. https://doi.org/10.1175/JCLI4202.1

13. Chang Y-S, Zhang S, Rosati A, Delworth TL, Stern WF (2013) An assessment of oceanic variability for 1960–2010 from the GFDL ensemble coupled data assimilation. Clim Dyn 40(3–4):775–803. https://doi.org/10.1007/s00382-012-1412-2

14. Czaja A, Frankignoul C (2002) Observed impact of Atlantic SST anomalies on the North Atlantic Oscillation. J Clim 15(6):606–623. https://doi.org/10.1175/1520-0442(2002)015<0606:OIOASA>2.0.CO;2

15. de Coëtlogon G, Frankignoul C (2003) The persistence of winter sea surface temperature in the North Atlantic. J Clim 16(9):1364–1377. https://doi.org/10.1175/1520-0442(2003)16<1364:TPOWSS>2.0.CO;2

16. Deser C, Alexander MA, Timlin MS (2003) Understanding the persistence of sea surface temperature anomalies in midlatitudes. J Clim 16(1):57–72. https://doi.org/10.1175/1520-0442(2003)016<0057:UTPOSS>2.0.CO;2

17. Frankignoul C, Kestenare E, Reverdin G (2021) Sea surface salinity reemergence in an updated North Atlantic in-situ salinity dataset. J Clim 34(22):9007–90023. https://doi.org/10.1175/JCLI-D-20-0840.1.

18. Gámiz-Fortis S, Pozo-Vázquez D, Esteban-Parra M, Castro-Díez Y (2002) Spectral characteristics and predictability of the NAO assessed through Singular Spectral Analysis. J Geophys Res 107(D23):4685. https://doi.org/10.1029/2001JD001436.

19. Garric G, Parent L, Greiner E, Drévillon M, Hamon M, Lellouche J-M, Régnier C, Desportes C, Le Galloudec O, Bricaud C, Drillet Y, Hernandez F, Le Traon P-Y (2017) Performance and quality assessment of the global ocean

574 eddy-permitting physical reanalysis GLORYS2V4 // EGU General Assembly
575 Conference Abstracts. V. 19. P. 18776.
576 20. Geiss A, Marchand R, Thompson LA (2020) The influence of sea
577 surface temperature reemergence on marine stratiform cloud. Geophys Res Lett
578 47(9):e2020GL086957. https://doi.org/10.1029/2020GL086957
579 21. Good SA, Martin MJ, Rayner NA (2013) EN4: quality controlled
580 ocean temperature and salinity profiles and monthly objective analyses with
581 uncertainty estimates. J Geophys Res Ocean 118(12):6704–6716.
582 https://doi.org/10.1002/2013JC009067
583 22. Gouretski V, Reseghetti F (2010) On depth and temperature biases in
584 bathythermograph data: development of a new correction scheme based on
585 analysis of a global ocean database. Deep Sea Res Part I 57(6):812–833.
586 https://doi.org/10.1016/j.dsr.2010.03.011
587 23. Grist JP, Sinha, B, Hewitt HT, Duchez A, MacLachlan C, Hyder P,
588 Josey SA, Hirschi JJM, Blaker AT, New AL, Scaife AA, Roberts CD (2019) Re-
589 emergence of North Atlantic subsurface ocean temperature anomalies in a seasonal
590 forecast system. Clim Dyn 53(7):4799–4820 https://doi.org/10.1007/s00382-019-
591 04826-w
592 24. Hanawa K, Sugimoto S (2004) «Reemergence» areas of winter sea
593 surface temperature anomalies in the world's oceans. Geophys Res Lett
594 31(10):L10303. https://doi.org/10.1029/2004GL019904
595 25. Hurrell JW, Deser C (2010) North Atlantic climate variability: the role
596 of the North Atlantic Oscillation. J Mar Syst 79(3–4):231–244.
597 https://doi.org/10.1016/j.jmarsys.2009.11.002
598 26. Ishii M, Kimoto M, Kachi M (2003) Historical ocean subsurface
599 temperature analysis with error estimates. Mon Weather Rev 131(1):51–73.
600 https://doi.org/10.1175/1520-0493(2003)131<0051:HOSTAW>2.0.CO;2
601 27. Köhl A (2020) Evaluating the GECCO3 1948–2018 ocean synthesis–a
602 configuration for initializing the MPI-ESM climate model. Q J R Meteorol Soc
603 146(730):2250–2273. https://doi.org/10.1002/qj.3790
604 28. Namias J, Born RM (1970) Temporal coherence in North Pacific sea-
605 surface temperature patterns. J Geophys Res 75(30):5952–5955.
606 https://doi.org/10.1029/JC075i030p05952

607 29. Newman M, Alexander MA, Ault TR, Cobb KM, Deser C, Di
608 Lorenzo E, Mantua NJ, Miller AJ, Minobe S, Nakamura H, Schneider N, Vimont
609 DJ, Phillips AS, Scott JD, Smith CA (2016) The Pacific decadal oscillation,
610 revisited. J Clim 29(12):4399–4427. https://doi.org/10.1175/JCLI-D-15-0508.1
611 30. Sugimoto S, Hanawa K (2005a) Why does reemergence of winter sea
612 surface temperature anomalies not occur in eastern mode water areas? Geophys
613 Res Lett 32(15):L15608. https://doi.org/10.1029/2005GL022968
614 31. Sugimoto S, Hanawa K (2005b) Remote reemergence areas of winter
615 sea surface temperature anomalies in the North Pacific // Geophys Res Lett. V. 32.
616 № 1. P. L01606. https://doi.org/10.1029/2004GL021410
617 32. Sukhonos PA, Diansky NA (2021) Analysis of the reemergence of
618 winter anomalies of upper ocean characteristics in the North Atlantic from
619 reanalysis data. Izv Atmos Ocean Phys 57(3):310–320.
620 https://doi.org/10.1134/S0001433821030099
621 33. Taws SL, Marsh R, Wells NC, Hirschi J (2011) Re-emerging ocean
622 temperature anomalies in late-2010 associated with a repeat negative NAO.
623 Geophys Res Lett 38(20):L20601. https://doi.org/10.1029/2011GL048978
624 34. Timlin MS, Alexander MA, Deser C (2002) On the reemergence of
625 North Atlantic SST anomalies. J Clim 15(18):2707–2712.
626 https://doi.org/10.1175/1520-0442(2002)015<2707:OTRONA>2.0.CO;2
627 35. Watanabe M, Kimoto M (2000) On the persistence of decadal SST
628 anomalies in the North Atlantic. J Clim 13(16):3017–3028.
629 https://doi.org/10.1175/1520-0442(2000)013<3017:OTPODS>2.0.CO;2
630 36. Zhao B, Haine TWN (2005) On processes controlling seasonal North
631 Atlantic sea surface temperature anomalies in ocean models. Ocean Modelling
632 9(3):211–229. https://doi.org/10.1016/j.ocemod.2004.05.001
633 37. Zhao X, Li J. (2010) Winter-to-winter recurrence of SSTA in the
634 Northern Hemisphere. J Clim 23(14):3835–3854.
635 https://doi.org/10.1175/2009JCLI2583.1
636 38. Zuo H, Balmaseda MA, Tietsche S, Mogensen K, Mayer M (2019)
637 The ECMWF operational ensemble reanalysis–analysis system for ocean and sea
638 ice: a description of the system and assessment. Ocean Sci 15(3):779–808.
639 https://doi.org/10.5194/os-15-779-2019
640

Tables

Table 1 The available period and depth of the summer seasonal thermocline and layers above and below the summer seasonal thermocline and the variance of temperature anomalies in the summer seasonal thermocline in the North Atlantic (15°N–70°N 80°W–8°W) explained by the leading EOF according to the data sets used.

	ISHII	EN4	SODA 2.1.6	ORA-S4	ORA-S3	GECCO3	GFDL	GODAS	GLORYS	ORA-S5	SODA 3.12.2
Available period	1945–2012	1945–2020	1958–2008	1958–2014	1959–2011	1948–2018	1961–2015	1980–2021	1993–2015	1979–2018	1980–2017
The depth above the thermocline, m	30	35–45	35–46	35–45	30–46	37–47	35–45	35–45	35–47	35–47	35–45
The depth under the thermocline, m	150	121–135	129–148	121–135	120–135	122–150	125–135	125–135	120–133	120–133	122–135
The depth of the summer seasonal thermocline, m	75–100	66–87	70–96	66–87	60–90	68–82	65–85	65–85	69–87	69–87	66–87
The percent variance explained by leading EOF, %	14.19	14.57	7.35	14.07	11.17	18.18	12.30	18.90	13.75	17.78	10.50

Table 2 The correlation coefficients between the time coefficients of the leading EOF of temperature anomalies in the summer seasonal thermocline in the North Atlantic (15°N–70°N 80°W–8°W) according to the data used for the overlapping period. Correlation coefficients in bold are significant at the 99% confidence level. Correlation coefficients marked with an asterisk are significant at the 95% confidence level.

	ISHII	EN4	SODA 2.1.6	ORA-S4	ORA-S3	GECCO3	GFDL	GODAS	GLORYS	ORA-S5	SODA 3.12.2
ISHII	1	**0.68**	0.42*	0.51*	**0.75**	0.52*	0.56*	**0.58**	0.60*	0.42*	0.68*
EN4		1	0.44*	**0.64**	**0.60**	**0.83**	**0.73**	0.40*	**0.93**	**0.80**	**0.94**
SODA 2.1.6			1	0.34	0.50*	0.38*	0.46*	0.12	0.31	0.01	0.33
ORA-S4				1	**0.72**	**0.65**	**0.82**	0.33	**0.73**	**0.84**	**0.79**
ORA-S3					1	0.54*	**0.71**	**0.54**	0.39	0.52*	**0.67**
GECCO3						1	**0.67**	0.31	**0.92**	**0.74**	**0.82**
GFDL							1	0.26	**0.89**	**0.69**	**0.85**
GODAS								1	0.23	0.47*	0.51*
GLORYS									1	**0.67**	**0.94**
ORA-S5										1	**0.83**
SODA 3.12.2											1

Table 3 The correlation coefficients between the time coefficients of the leading EOF of temperature anomalies in the summer seasonal thermocline in the North Atlantic (15°N–70°N 80°W–8°W) according to the data used and the NAO index in previous February, the NAO index averaged over previous January–February, the NAO index averaged over previous January–February–March for the overlapping period. Correlation coefficients in bold are significant at the 99% confidence level. Correlation coefficients marked with an asterisk are significant at the 95% confidence level.

	ISHII	EN4	SODA 2.1.6	ORA-S4	ORA-S3	GECCO3	GFDL	GODAS	GLORYS	ORA-S5	SODA 3.12.2
The NAO index in previous February	0.28	0.46*	0.36*	0.26	0.33	0.39*	0.46*	0.16	0.58*	0.32	0.43*
The NAO index averaged over previous Jan-Feb	0.33	0.48*	0.35	0.28	0.37*	0.43*	0.52*	0.10	**0.67**	0.39*	0.47*
The NAO index averaged over previous Jan-Feb-Mar	0.36*	0.52*	0.26	0.33	0.40*	0.45*	0.54*	0.08	**0.71**	0.49*	0.57*

Figures

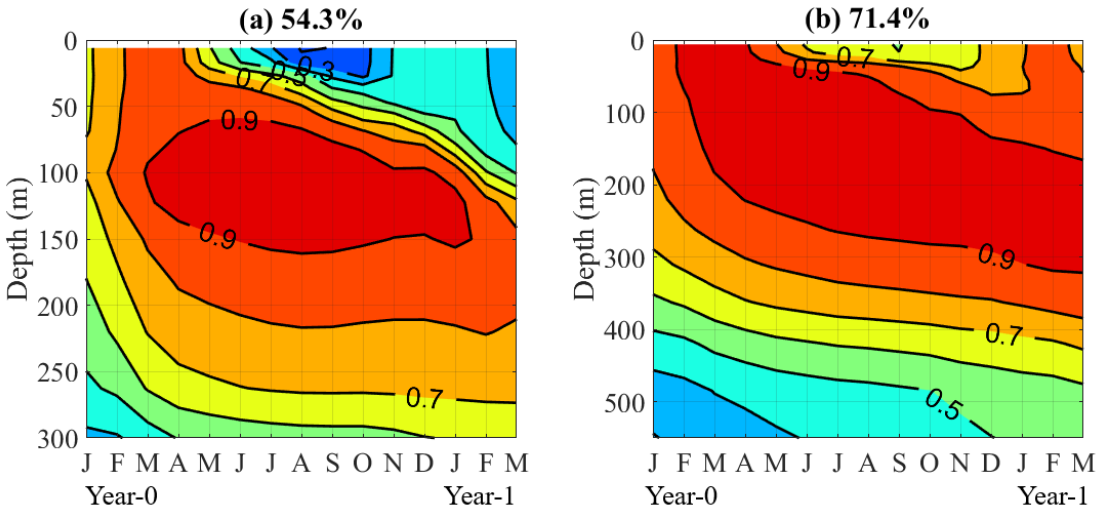

Fig. 1 Time–depth pattern of the leading EOF for (a) the Sargasso Sea (25°–35° N, 65°–45° W) and (b) the northeast Atlantic (35°–60° N, 45°–8° W) regions from GECCO3 data for the period 1948–2017. The value at the top of each panel is the fraction of the variance explained by this EOF. EOF calculation was performed from January to March of the following year and from the surface to a depth of 300 m (a) and 550 m (b). The EOF pattern is shown as the correlation between the principal component record and temperature anomaly time series for the available period. Contour interval is 0.1.

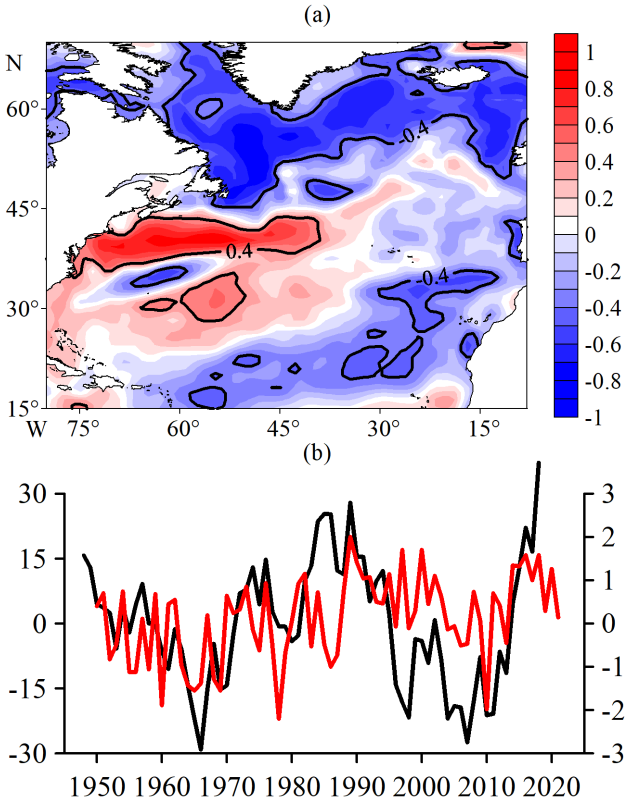

Fig. 2 (a) Spatial structure of the leading EOF of the anomalous temperature field during August–September between 68–82 m depth; (b) corresponding time coefficient in the GECCO3 data for the period 1948–2018 (black curve, left scale) and the NAO index in previous February for the period 1950–2021 (red curve, right scale). The EOF domain is 15°N–70°N and 80°W–8°W in the North Atlantic. Third–order polynomials are removed. The spatial EOF pattern is shown as the correlation between the time coefficient and temperature anomalies for the period available. The fill is drawn through 0.1. Isolines ±0.4 are plotted.

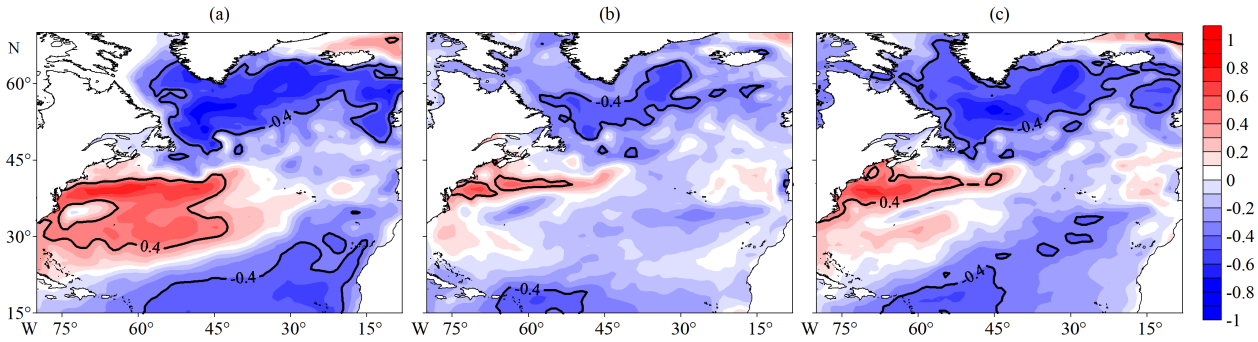

Fig. 3 Correlations between the timeseries of dominant temperature anomaly pattern in the summer seasonal thermocline and gridded SSTA from the GECCO3 data for the period 1948–2018 in (a) March, (b) September, and (c) November of the same year. Isolines ±0.4 are shown.

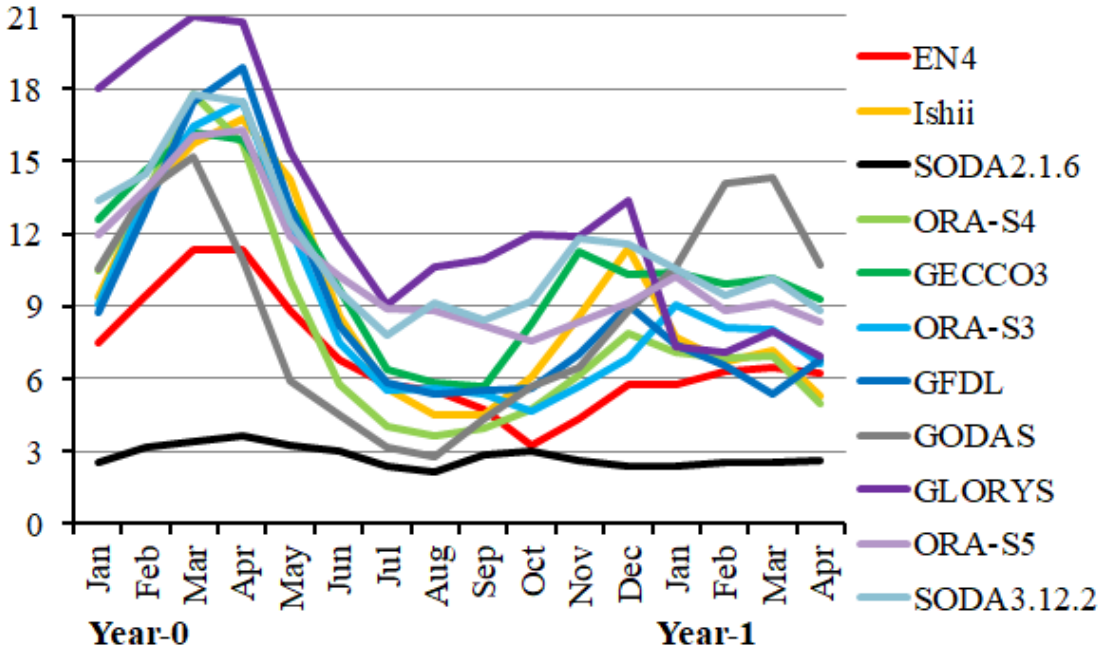

Fig. 4 The percent variance of the SSTA between 15°N–70°N and 80°W–8°W in the North Atlantic explained by leading EOF in the summer seasonal thermocline, as a function of calendar month, from the previous January to the following April for the available period in each data set.

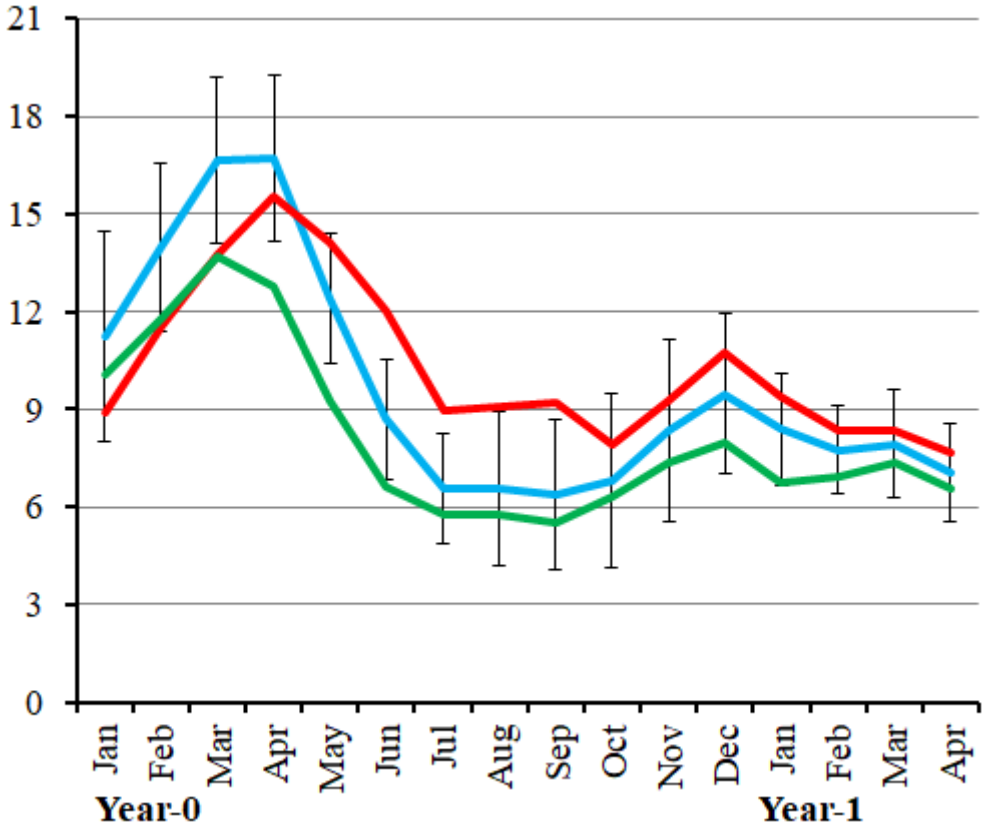

Fig. 5 The average across datasets used percent variance of the SSTA between 15°N–70°N and 80°W–8°W in the North Atlantic explained by leading EOF in the layer above the summer seasonal thermocline (red line, without ISHII, SODA2.1.6 and GODAS data), in the summer seasonal thermocline (blue line and black vertical error bars, without SODA2.1.6 and GODAS data), in the layer under the summer seasonal thermocline (green line, without SODA2.1.6, ORA-S3 and GODAS data), as a function of calendar month, from the previous January to the following April. The black vertical error bars indicate ±1 standard deviation for the ensemble of datasets except for the SODA2.1.6 and GODAS reanalyses.

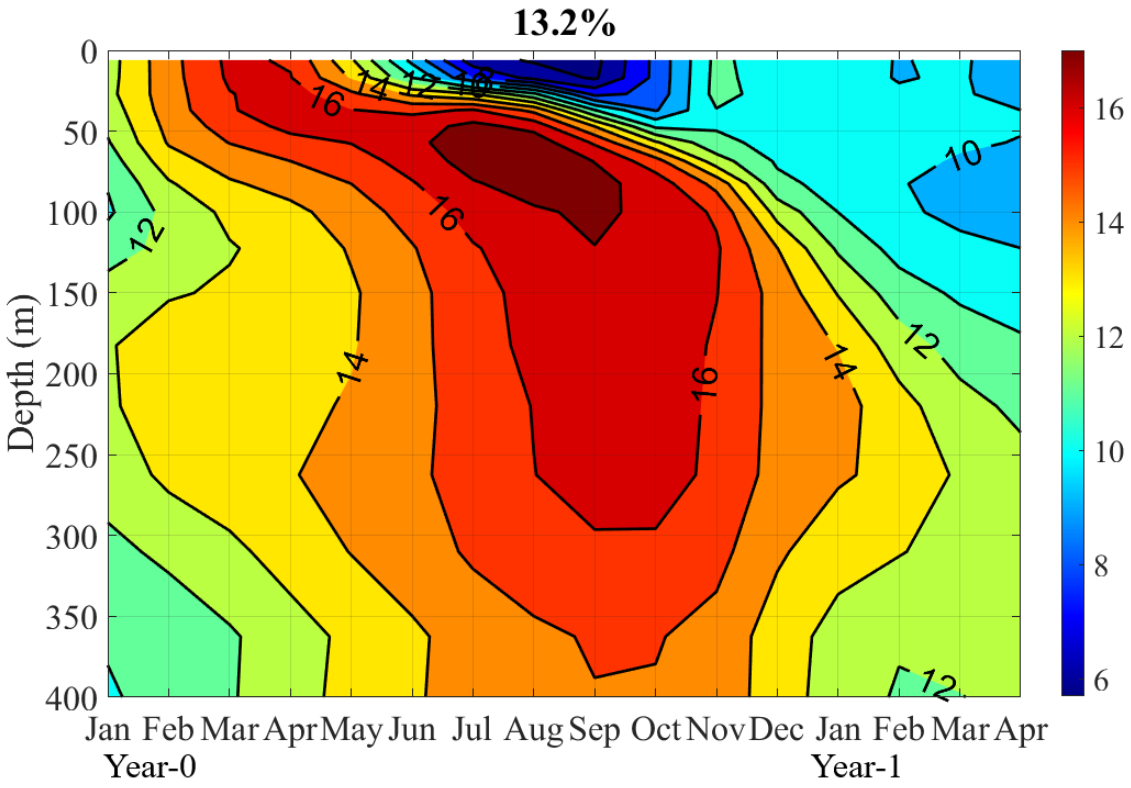

Fig. 6 The percent variance of the temperature anomalies between 15°N–70°N and 80°W–8°W in the North Atlantic explained by leading EOF in the summer seasonal thermocline as a function of calendar month and depth. Calculation was performed according to the GECCO3 data for the period 1948–2017, from the previous January to the following April and from the surface to a depth of 400 m (16 levels). The value at the top of panel is the fraction of the variance explained by this EOF.

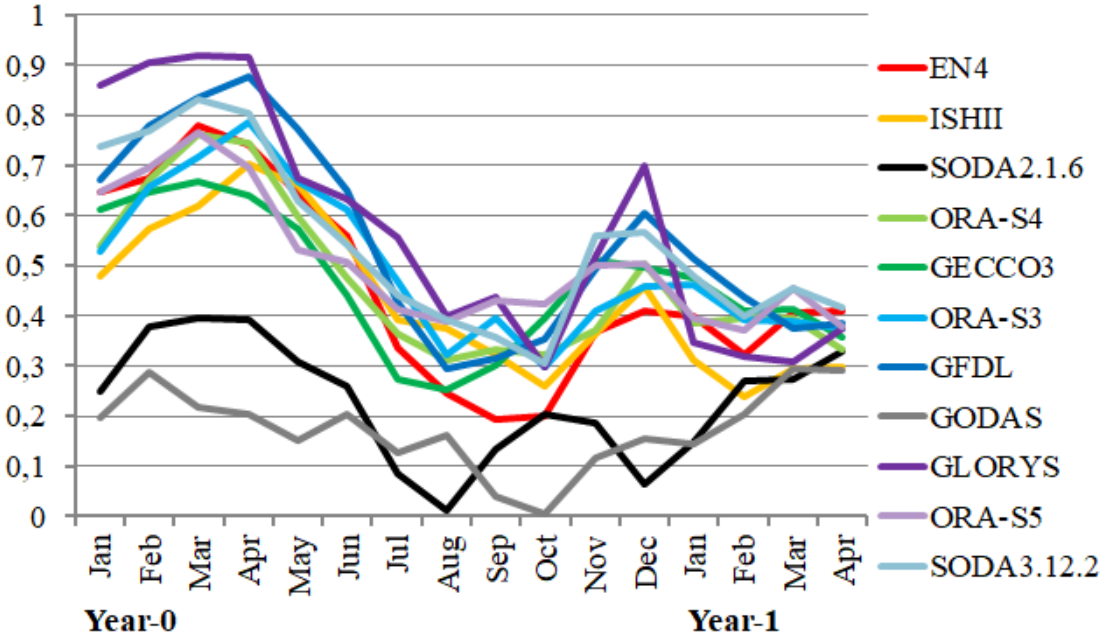

Fig. 7 Correlation coefficients between the time coefficient of the leading EOF of the SSTA between 15°N–70°N and 80°W–8°W in the North Atlantic, calculated separately for each month, and the time coefficient of the EOF of temperature anomalies in the summer seasonal thermocline in August–September from the previous January to the following April for the available periods in each data set.

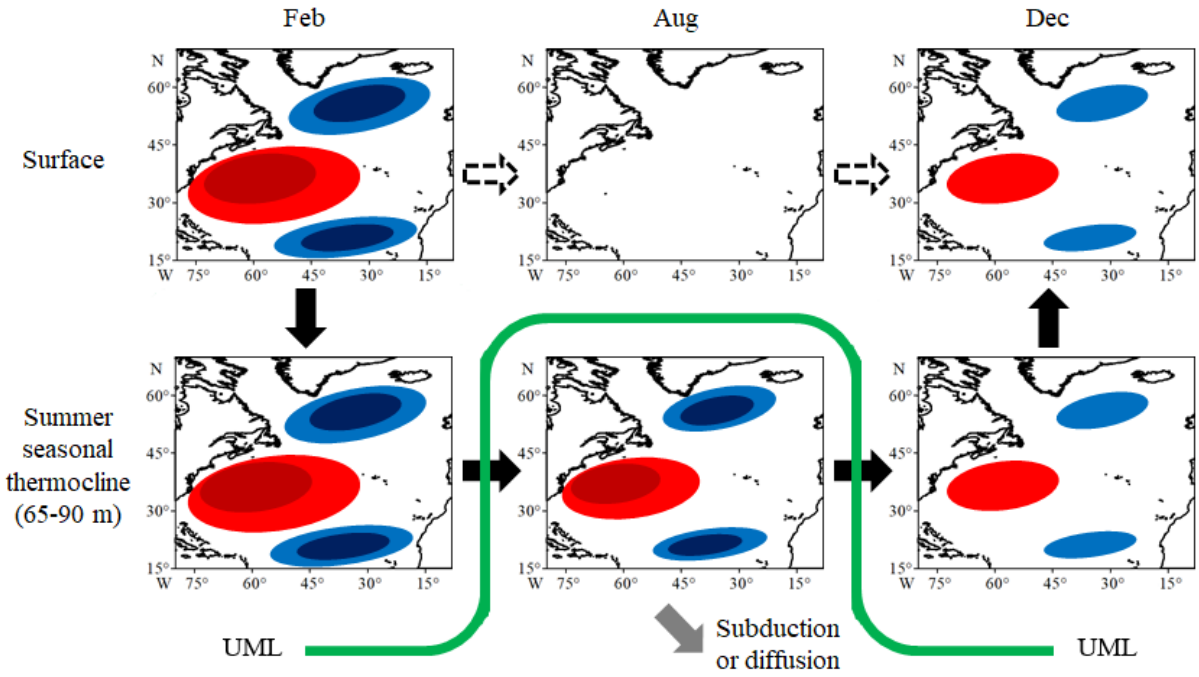

Fig. 8 Schematic representation of the SSTA tripole reemergence process in the North Atlantic (15°–70°N 8°–80°W). Positive and negative temperature anomalies (related to the NAO positive phase; for the NAO negative phase, the signs of the anomalies are opposite) associated with the tripole pattern are represented by the red and blue ovals. The size of the ovals determines the area of the anomalies, and the color determines their amplitude (dark red (dark blue) corresponds to positive (negative) anomalies of stronger amplitude). The black arrows show the path of reemergence. The white dotted arrows show the state of the ocean surface. The gray arrow denotes diffusion and subduction processes that reduce the amplitude and area of temperature anomalies by almost a third. The thick smooth green line is the UML depth annual cycle.